

Quantum-Assisted Optical Interferometry

Alex Parsells and Jonathan Schiff

April 2021

Abstract

Traditional astronomical interferometers are best suited to longer wavelengths, since observing shorter wavelengths (e.g. optical) requires a complicated and expensive physical connecting path between stations, limiting baseline size. In a recent paper, Stankus et al. [arXiv:2010.09100 (2020)] proposed a novel design for an optical interferometer that takes advantage of two photon correlation effects to eliminate the need for a connecting path and thus achieve arbitrary baselines and angular resolution. The proposed instrument would be capable of taking precise astrometric data with many applications to astrophysics and cosmology. Two interference effects are integral to the instrument’s operation: the Hanbury Brown and Twiss (HBT) effect and the closely related two-photon amplitude interference effect. Experiments with simulated starlight are ongoing to test the principles behind the instrument. The current state of experimentation and analysis has clearly demonstrated the HBT effect in the laboratory, and has led to a $3.88 \pm 0.92 \sigma$ certainty that the two-photon amplitude interference effect has been observed as well. Forthcoming laboratory experiments will improve the statistical certainty that the two-photon amplitude interference effect has been observed and will pave the way for sky testing with on astronomical sources.

1 Introduction

The angular resolution of a telescope is diffraction limited and obeys the relationship $\theta \sim \frac{\lambda}{D}$, where θ is the angular resolution, λ is the wavelength of the light observed and D is the diameter of the telescope. Therefore, an increase in telescope diameter or an observation at shorter wavelengths improves angular resolution. Astronomical interferometers accomplish the latter option by using at least two smaller telescopes separated by a baseline distance, labeled B . Light from each station is interfered, and the interference (“fringe”) pattern produced is sensitive to the difference in the path length traveled by the light to one station versus

the other. In this scheme, the angular resolution is now given by $\theta \sim \frac{\lambda}{B}$. Interferometers create a network of telescopes with an effective diameter equal to their baseline separation, which can be made much larger than the diameter of any single telescope (up to several thousand kilometers for radio interferometers).

Classical interferometers work best for observing longer wavelengths (e.g., radio) because at these wavelengths, the entire wavefront can be captured and recorded in real time as they arrive, and the phase and time of arrival of each photon can be stored on hard drives and interfered later. This technique does not work for short wavelengths (e.g., optical), which instead require a live physical connecting path between stations so that the light can be brought together and interfered. Such a path's length must be accurate to less than one wavelength of the light observed, making its construction very difficult and expensive. These difficulties have limited present-day optical interferometers to $B \sim 100$ m, a far cry from the thousand-km baselines achieved by radio interferometers. An optical interferometer with a baseline comparable to that of the largest radio interferometers would achieve resolution improved by several orders of magnitude over these radio interferometers due to the shorter wavelengths involved.

In a recent paper, Stankus et al. [1] put forth a design for a new type of long-baseline optical interferometer (Fig. 1), one that would interfere two photons from two different astronomical sources instead of the traditional single photon. This design would utilize correlation effects between the two photons to bypass the need for a physical connecting path between stations. In particular, the basis of this telescope is a phase-dependent effect henceforth called two-photon amplitude interference. This effect is related to and appears in conjunction with the well-known Hanbury Brown and Twiss (HBT) effect [2]. The two-photon amplitude interference effect eliminates the requirement for a live connecting path between detector stations. Instead, local measurements of the time of arrival of photons can be made at each station, and the pattern of photon coincidences (i.e., when two photons enter two different detector branches at or near the same time), can be analyzed afterward. Correlations in coincident photon detections between detectors in different observation sites is sensitive to the sky angle between the two astronomical sources. This process is discussed more in section 2.1 below.

Because the stations of the telescope do not need to be physically connected, they can be separated by an arbitrary distance. Such an instrument would therefore be able to achieve arbitrarily good angular resolution and would be capable of generating precise astrometric data on par with that of the Gaia satellite. The applications for this type of data are myriad and include studies of dark matter, general relativity near black holes, and the Hubble constant [1].

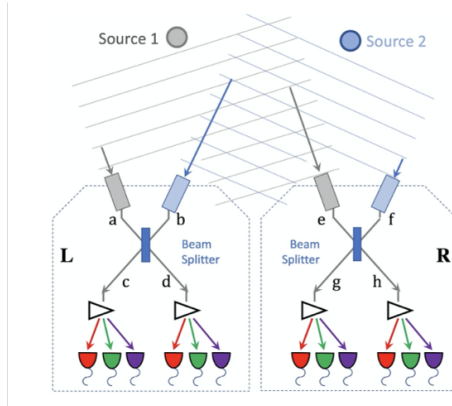


Figure 1: Sketch of two-photon amplitude interferometer observing two astronomical sources. Photons from each source, shown as plane waves, are incident on each detection site, labeled L and R, which is equipped with a pair of telescopes. The detected light is sent to a beam splitter and then diffracted into spectroscopic bins and read out by single photon detectors. . Figure taken from [1] (with permission)

Our group has built a laboratory mockup of the Stankus et al. [1] telescope design using lamps and superconducting nanowire detectors (SNSPDs). In this paper, we describe ongoing experimental tests of the design. These include analyzing photon coincidence data from our mockup and comparing the results to statistical simulations to determine the significance of the photon correlations we observe. We also describe tests made with the fast optical camera Tpx3Cam, another candidate for the telescope’s photon detectors. We discuss the theoretical background of our experiment and our expected observables in detail in the next section.

2 Proof-of-concept Testing

2.1 Motivation and background

A diagram of the proposed design for the two-photon interferometer is shown in Figure 1. In the simplest implementation, two telescope sites, observing two astronomical sources, are separated by a baseline distance, B . Incident light from the sky sources passes through a 50-50 beam splitter at each detection site, is diffracted into fine spectroscopic bins (for example, using an echelle grating), and is then detected by fast single photon detectors. With a reasonable implementation of the proposed interferometer for a single night’s observation on a bright stellar source, the instrument would be able to achieve an impressive $10 \mu\text{as}$ resolution [1]. A photodetection and full quantum field theory-based analysis reveals that the pattern of coincidences between

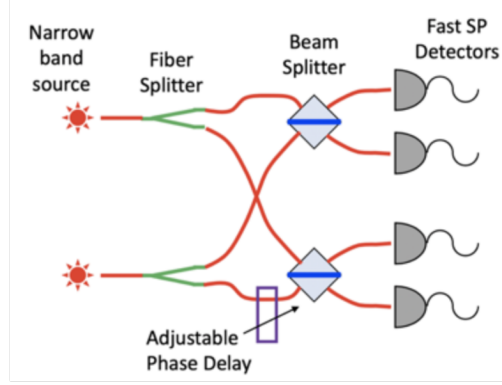


Figure 2: A sketch of the lab setup to test the two-photon amplitude interference effect. Argon lamps are used to approximate a narrow spectral bin from a thermal source. The light from each argon lamp is split by a fiber splitter and sent to one of two beam splitters. The output fibers from the beam splitters are attached to four SNSPDs. An adjustable phase delay is inserted on one arm of the apparatus. Figure taken from [3] (with permission)

channels is sensitive to the opening angle between the two observed sources in a real sky observation. [1] Here, we will restrict our discussion to the most relevant aspects of this theory for proof of concept laboratory testing with the setup shown in Figure 2.

Our telescope design as proposed in [1] would record the arrival time of every photon entering its detectors. The HBT effect predicts that a histogram of the elapsed time (dT) of consecutive photon hits between any given pair of channels (coincidence distribution), would have a peak at a particular value of dT that corresponds to the photons arriving in the same temporal mode. Figure 3 shows one such basic coincidence distribution between photon hits in two channels of our lab mockup. Throughout this paper, we refer to two regions in the coincidence distributions such as the one shown in Figure 3: 1) the peak region, the region in which the HBT enhancement in coincidences is observed; and 2) the normalization region, a region outside of the peak in which coincidences are simply due to the combinatorics of single-channel rates of photon detection (see Figures 3 and 6). Theoretical calculations from [1] yield Eq. (1) for the number of expected coincidences in the peak region:

$$\langle N(xy) \rangle(t) = \overline{N(xy)} [1 \pm V(xy) \cos(\Delta\delta(t))] \quad (1)$$

where $x, y \in \{\{1, 3\}, \{1, 4\}, \{2, 3\}, \{2, 4\}\}$ are the detection channel pairs of interest, $\langle N(xy) \rangle(t)$ is the number of peak coincidences as a function of time, $\overline{N(xy)}$ is the average number of peak coincidences, $V(xy)$ is the two-photon amplitude interference visibility, and $\Delta\delta(t)$ is the difference in phase differences between photons

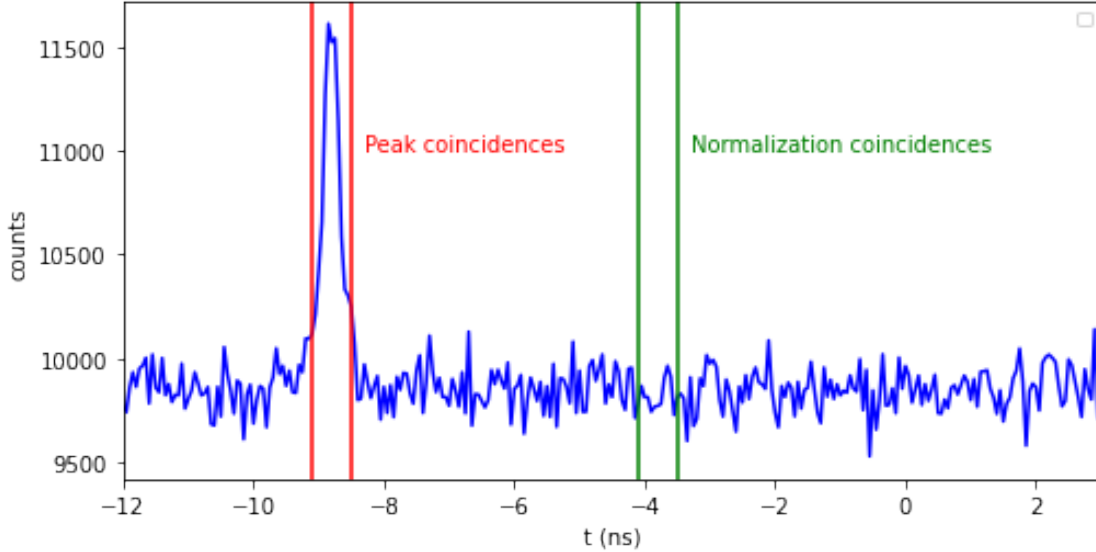


Figure 3: A sample plot of the coincidence distribution between two channels taken from a 70 minute experiment in which the schematic from Figure 2 is implemented with four SNSPDs as the single photon detectors. The HBT peak in this figure is characteristic of that which is observed in all six channel combinations.

from each source arriving at each station. (Each photon will arrive in a different phase at the two stations due to the path length difference from a photon’s astronomical source to either station 1 or station 2.) Note that the number of peak coincidences is dependent on this difference in phase differences, $\Delta\delta(t)$. Over a nightlong observation, $\Delta\delta(t)$ will oscillate from 0 to 2π many times as the rotation of the Earth causes the path length difference from the source to each station to change. As a result, $\langle N(xy) \rangle(t)$ will oscillate periodically, and the period of oscillation is a function of the sky angle between the two sources, producing precise astrometric data. We call this oscillation two-photon amplitude interference (2PAI). In addition to the oscillation in coincidence counts for a given pair of channels, we also expect to see certain correlations and anticorrelations in these oscillations between different pairs of channels, which will be discussed further in the next section. [1] In our laboratory setup, $\langle N(xy) \rangle(t)$ is analogously sensitive to the path length difference between two pseudo-thermal narrow band sources and each pair of single-photon detectors, which can be controlled and varied with an adjustable phase delay to mimic the phase shift caused by Earth’s rotation. We will now turn to the statistical framework that allows us to test for the two-photon amplitude interference effect in the lab.

2.2 Statistical framework

As mentioned above, the two-photon amplitude interference effect introduces the oscillatory term in the number of peak coincidences in Equation (1). Here, we present three simulations of experimental conditions and the subsequent statistical analysis that can be implemented to glean from the data presented in the next section whether or not the two-photon amplitude interference effect is observed. Throughout our discussion, we refer to time intervals t_i , in which the phase is stable and unchanging, as trials. The three simulations are:

1. The two photon interference effect is not present, i.e. $V(xy) = 0$ or $\Delta\delta(t) = \pi$:

$$\langle N(xy) \rangle(t) = \overline{N(xy)} = \text{constant} \quad (2)$$

2. The phase is perfectly stable throughout the duration of the experiment and $\Delta\delta(t)$ cycles linearly in discrete increments, $d\delta$, from 0 to 2π :

$$\begin{aligned} \langle N(xy) \rangle(t_i) &= \overline{N(xy)} [1 \pm V(xy) \cos(\Delta\delta(t_i))] \\ \Delta\delta(t_i) &= (d\delta * t_i) \pmod{2\pi} \end{aligned} \quad (3)$$

3. The phase is not stable over long periods of time and varies from trial to trial, but is stable during each trial. In this case, $\Delta\delta(t) \in [0, 2\pi)$, but is a random value in this interval for each trial, t_i :

$$\begin{aligned} \langle N(xy) \rangle(t_i) &= \overline{N(xy)} [1 \pm V(xy) \cos(\Delta\delta(t_i))] \\ \Delta\delta(t_i) &\text{ is randomly drawn from a uniform distribution } [0, 2\pi) \end{aligned} \quad (4)$$

For simplicity, we initially assume that each channel combination has the same mean peak coincidence rate, $\overline{N(xy)} = \overline{N}$, and the same two photon amplitude visibility, $V(xy) = V_{2PS}$. Therefore, when Equation (1) is written out explicitly for each channel combination of interest we obtain:

$$\begin{aligned} \langle N(13) \rangle(t) &= \overline{N} [1 + V_{2PS} \cos(\Delta\delta(t))] \\ \langle N(14) \rangle(t) &= \overline{N} [1 - V_{2PS} \cos(\Delta\delta(t))] \\ \langle N(23) \rangle(t) &= \overline{N} [1 - V_{2PS} \cos(\Delta\delta(t))] \\ \langle N(24) \rangle(t) &= \overline{N} [1 + V_{2PS} \cos(\Delta\delta(t))] \end{aligned} \quad (5)$$

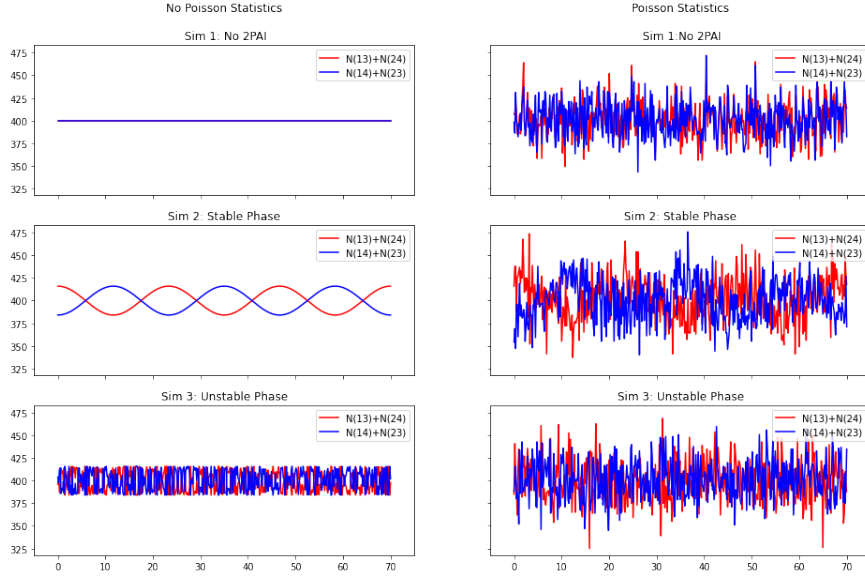


Figure 4: Left: Results from each simulated experiment when Poisson fluctuations are ignored. Right: Results from each simulated experiment when Poisson fluctuations are not ignored.

Equation 5 shows that, under a stable and linearly increasing phase (i.e. simulation number 2), the rates of coincidences in channels 1&3 and 2&4 will oscillate in phase with each other and the coincidence rates in channels 1&4 and 2&3 will oscillate in phase with each other, but 180° out of phase with those from channels 1&3 and 2&4. Since the photon rates are in reality not constant but follow a Poissonian distribution, Figure 4 shows the results from simulations of each experimental condition with and without Poisson noise included. To match the parameters of ongoing experiments, we assume a 70-minute experiment with each trial lasting 10 s, such that we have a total of 420 trials over the duration of the experiment. We initially set $\bar{N} = 200$, $V_{2PS} = 0.04$ as a first approximation since these values are representative of what we see in our real data. Fine-tuning of these parameters is discussed in the next section.

Not only is Figure 4 useful in qualitatively showing the expected shape of the peak coincidence rates under different experimental circumstances, but the results of each simulation can also be used to quantitatively predict the correlations between coincidence rates that we expect under different experimental conditions. The statistical quantity of interest to achieve this is the Pearson correlation coefficient:

$$r(\mathbf{x}, \mathbf{y}) = \frac{\sum_i^N (x_i - \bar{x})(y_i - \bar{y})}{\sqrt{\sum_i^N (x_i - \bar{x})^2 \sum_i^N (y_i - \bar{y})^2}} \quad (6)$$

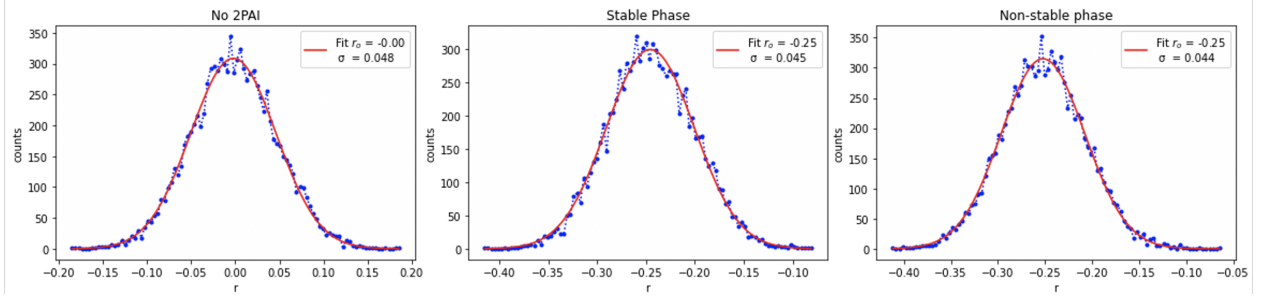


Figure 5: Gaussian fit from 10,000 simulations of experiments with Left: No two-photon amplitude interference. Center: Stable phase over the duration of the experiment. Right: Non-stable phase from trial to trial within experiment.

where \mathbf{x}, \mathbf{y} are arrays of the number of coincidences for each trial for each pair of channel combinations that oscillate in phase. Namely:

$$\begin{aligned} \mathbf{x} &= N(13)(t) + N(24)(t) \\ \mathbf{y} &= N(14)(t) + N(23)(t) \end{aligned} \tag{7}$$

It can be shown that, when Poisson statistics are ignored, experiments in which there is no two-photon amplitude interference have a Pearson $r(\mathbf{x}, \mathbf{y})$ value of 0 and experiments in which the two-photon amplitude interference effect is present (irrespective of phase stability) have $r(\mathbf{x}, \mathbf{y}) = -1$. When each experimental circumstance is simulated 10,000 times with Poisson statistics included, we obtain a distribution of r values, which provide an expected/mean correlation coefficient r_o and standard deviation σ for each experimental condition. These distributions, fit with a Gaussian, are shown in Figure 5. Note that the distribution has a mean of 0 in the no-2PAI case but has a mean of -0.25 in both of the cases with 2PAI, which together with the relatively small standard deviations indicates a statistically significant anticorrelation. This is the behavior we expect to see from the real data that we discuss in the next section.

With this framework in place, we turn to real experimental data in which SNSPDs are used as the single-photon detectors. In the next section, we adjust simulation parameters to better approximate experimental conditions and analyze experimental data vis-a-vis the results from simulations.

2.3 Testing with SNSPDs

2.3.1 Background and setup

To test the phase-dependent oscillations in peak coincidences that are predicted by the two-photon amplitude interference effect, we conducted 70-minute-long experiments with the laboratory setup shown in Figure 2. SNSPDs have fast temporal resolution and high quantum efficiency, making them effective single photon detectors for our purposes. [3] [4]

Our current implementation of this setup is capable of phase stability on the order of 10 s, but not for the duration of the 70 minute experiment. The laboratory conditions therefore closely resemble the third simulation of experimental conditions detailed above. Therefore, in order to determine the statistical significance of the correlations observed in the experimental data, we compare experimental results to a null hypothesis in which there is no two-photon amplitude interference and to an alternative hypothesis which aligns with the third simulation described in the previous section.

2.3.2 Results

We will focus on a narrow set of results from the setup depicted in Figure 2, but more comprehensive results from this and other setups can be found in Appendix B. Figure 6 shows the rates of peak coincidences and normalization coincidences from this experiment. It is clear that the peak coincidences have a mean rate that is larger than that of the normalization coincidences, as expected from the HBT enhancement (see B.5.2 for further discussion on fluctuations in the normalization region). Therefore, we are confident that we have observed the HBT effect in this data.

To determine whether we also see 2PAI in this data, it is useful to compare the data to simulations in which the mean peak coincidences are chosen to match the experimental data. The actual experimental conditions most closely resemble the third simulation circumstance, in which the phase is stable in 10 s increments but randomly changes between these increments.

The phase instability precludes our ability to utilize the oscillatory behavior of peak pair rates to verify the two-photon amplitude interference effect. Instead, we utilize the Pearson correlation coefficient $r(\mathbf{x}, \mathbf{y})$, with \mathbf{x} and \mathbf{y} defined according to Equation (7), and compare experimental results to simulations. For 10 s integration times (i.e. 420 trials over the duration of the experiment), the measured correlation coefficient is $r(\mathbf{x}, \mathbf{y}) = -0.189 \pm 0.045$ (for details on the error propagation on r , see Appendix A). The

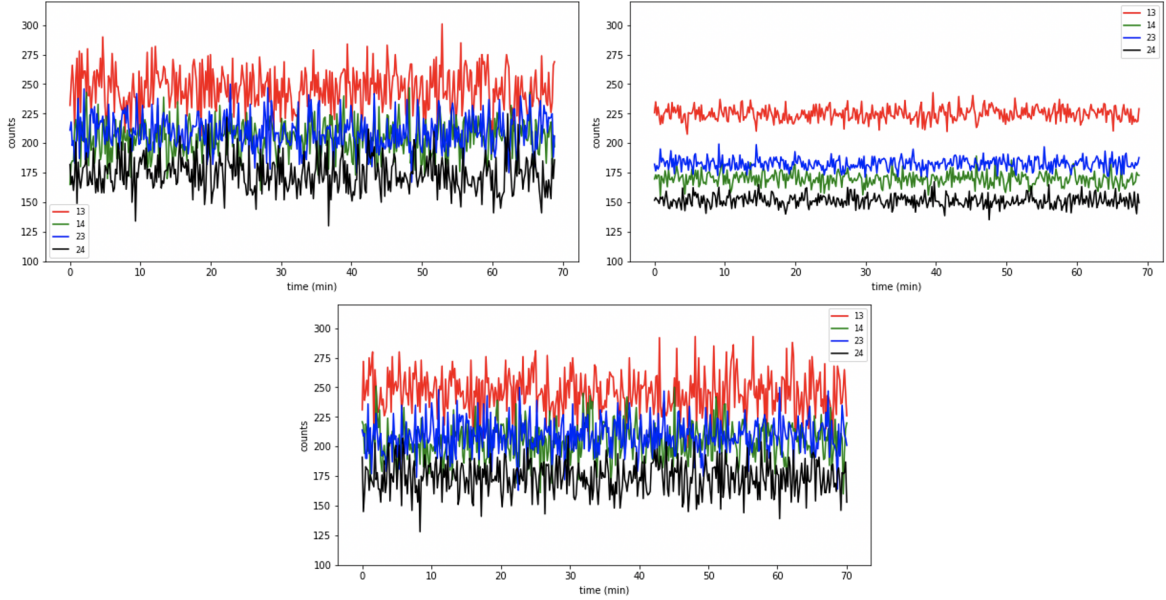


Figure 6: Top: Results from 70 minutes experimental data. Top Left: Peak coincidence rates Top Right: Normalization coincidence rates. Bottom: Simulated data (The mean for each peak distribution was set equal to the mean from the real data. V was set to 0.03 across all channel combinations)

expected correlation coefficient and standard deviation found when the null and alternative hypotheses are simulated 10,000 times are shown in Figure 7. We can see that our observed r is $3.88 \pm 0.92 \sigma$ from the mean given by the null hypothesis and $0.85 \pm 0.96 \sigma$ from that given by the alternative hypothesis. These results give us a high degree of confidence that our observed r is not due to statistical fluctuations from a null result. Moreover, the observed r value is within one standard deviation of the expected correlation coefficient from the alternative hypothesis. Although further experimental testing and refinement of the simulations is necessary to fully determine that we have observed 2PAI, these preliminary results strongly suggest that we have. Improved phase control over the duration of the experiment is necessary to observe periodic oscillation in the peak pair rates (as opposed to only a statistical anticorrelation), which is key to achieving high levels of astrometric precision. This experimental work is ongoing.

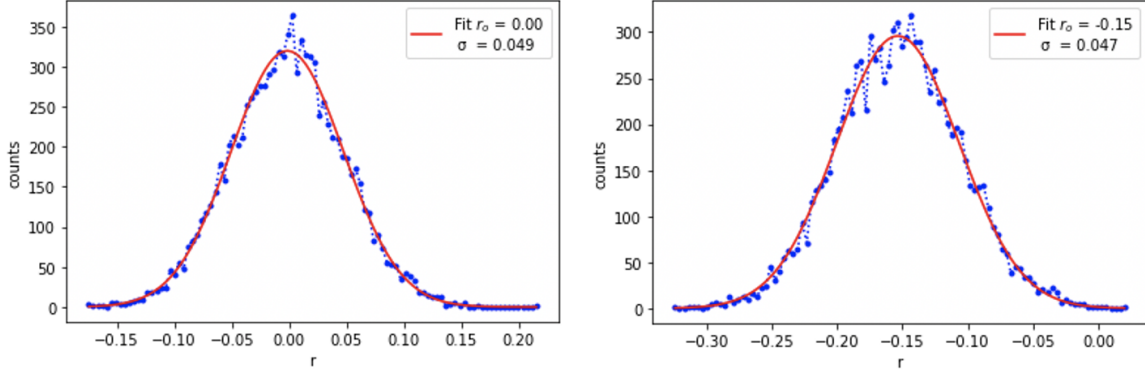


Figure 7: Distribution of correlation coefficient values from 10,000 simulations, fit with Gaussian to estimate the expected correlation coefficient and its standard deviation. Right: Results from the null hypothesis Left: Results from the alternative hypothesis.

2.4 Testing with Tpx3Cam fast optical camera

2.4.1 Background and setup

In addition to the tests with SNSPDs described above, we also conducted tests of our setup with the fast optical camera Tpx3Cam in conjunction with an image intensifier as the photon detector. Tpx3Cam is a 256x256 square pixel camera that can record the location, time of arrival (ToA), and time over threshold (ToT; a proxy for brightness) of every photon incident on the camera [5]. It records ToA with 1.56-ns granularity and ToT with 25-ns granularity. The intensifier contains a fast scintillator and makes Tpx3Cam single-photon-sensitive.

The setup used for these tests is shown in Fig. ???. Pseudothermal light is emitted from an argon lamp, which releases many photons continuously to pass through the apparatus. The light is then split into two optical fibers, which are connected to the intensifier. When a photon hits the intensifier, the scintillator releases additional photons, which are then detected by Tpx3Cam. Since the two optical fibers are fixed with respect to the pixel array, the incident photons are focused into two regions of interest on the camera, each of which is roughly 20x20 square pixels and which we colloquially call "channels" 1 and 2. The camera's pixel array then records the time and pixel of each incident photon, and a clustering algorithm puts groups of nearby photons into clusters (see Fig. 8) that allow us to reconstruct the location and ToA of the original photons from each channel. Data from the experiment can be exported as a CSV file in which each line is

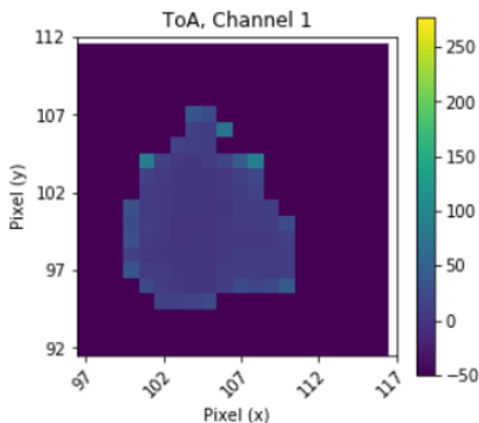


Figure 8: Illustration of the Tpx3Cam clustering algorithm. This is a zoomed-in view of the camera’s pixels, showing where and when various photons from the scintillator hit the camera. This set of photons was grouped together by the camera’s algorithm into a single cluster, indicating that they all likely came from the same lamp photon when it hit the scintillator.

a cluster and contains information on that cluster’s location (x and y in pixels), ToA, ToT, and size (the number of pixels in that cluster).

A total of 26 datasets of this kind were recorded, each corresponding to a distinct run of the experiment. The runs varied in duration from 10 seconds to 5 minutes, and slightly more than half were taken with a mask, which suppresses data readout in all pixels outside the two regions of interest. Those runs that are taken without a mask are useful for constraining the natural dark count rate (i.e., noise) of the electronics and the environment. Finally, the runs also vary in their photon rates; i.e., in the intensity of the light. In the next section we attempt to find variation in the photon coincidence data with changes in photon rates. The combined rate of photons hitting the camera between channels 1 and 2 ranges from 46 kHz to 167 kHz.

Data from each run was analyzed to determine the time difference (dT) distribution between adjacent coincident photons; that is, the time difference between pairs of photons from different channels with ToA within a set duration of each other and no other incident photons with ToA in between. We varied the value of this duration (the maximum dT that is still plotted as a coincidence) from 50 ns to 20 μ s, creating several different histograms for each run. These distributions were fit with exponential curves to determine how well such a curve described the data. We expected that these dT histograms, similar to the analogous SNSPD dT histograms, would show clear peaks near $dT = 0$, representative of the HBT effect. Crucially, since the current camera setup has only two channels, we cannot look for 2PAI or any correlations between

pairs of channels in this data. The analysis also included basic data such as the location of each cluster, number of pixels per cluster, ToT data, and photon rates in each channel. Results of these experiments are presented in the next section.

2.4.2 Results

Nearly all dT distributions show clearly visible peaks at $dT = 0$, which seems to indicate that the HBT effect is present. See Fig. 9 for an example. Also see Fig. 10, where four of the distributions from Fig. 9 have been fitted with exponential curves. Note the central peaks in each plot, which appear to deviate from a pure exponential. We explore this more in Fig. 13 (see below).

We hypothesized that datasets with lower photon rates might show increased prominence in their central HBT peaks, because their exponential tails would be less steep and therefore more distinguishable from the Gaussian HBT peak. Hence in Fig. 11 we show dT histograms from five different datasets with combined photon rates of 46, 54, 110, 143, and 154 kHz. Also see Fig. 12 for the same plots with exponential fits overlaid. It does appear as though there is a negative correlation between photon rates and peak prominence, but further and more quantitative analysis is needed to confirm or deny this observation.

Finally, see Fig. 13, where the same data from Figs. 11 and 12 is plotted with the value of the fit at all x subtracted from it. This allows us to see clearly any deviations in the data from an exponential curve. We also changed the fitting algorithm such that it would no longer ignore the central ± 50 ns when finding the optimal fit parameters. We interpret the fact that the fit remains poor in the central region (note the large difference between the data and the fit inside ± 50 ns) as evidence that the HBT effect is present in the form of a Gaussian overlaid on top of the exponential.

2.5 Future plans

Future experiments are planned to confirm and build on the results presented here. Taking more data with the current setups and refining our statistical simulations will give more insight into the statistical significance of our observed two-photon amplitude interference. We also have a free-space nanowire setup (Fig. 14) in progress that will alleviate the phase stability and control issues that arose from vibrations in the optical fibers.

Beyond that, we are planning to conduct experiments on an 8-channel nanowire setup that could

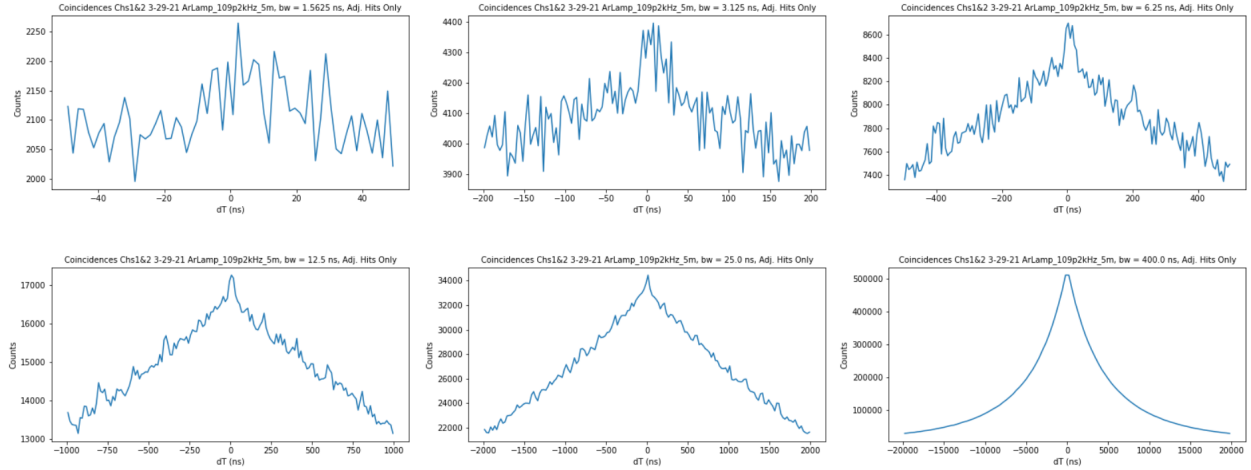


Figure 9: Example of the six coincidence dT distributions that were made for one particular run, which was masked, had combined photon rates of roughly 109 kHz, and lasted 5 minutes. Each subplot has a different range, which indicates the maximum ToA difference two consecutive and opposite-channel photons can have to be considered a coincidence; this maximum is either 50, 200, or 500 ns; 1, 2, or 20 μ s. Along with the range, we also vary the bin width used in the histogram to maintain very roughly equal numbers of bins throughout. Since the natural ToA granularity of Tpx3Cam is 1.5625 ns, all bin widths are multiples of this value. Note the small central peak, which looks roughly Gaussian, laid on top of the decaying exponential—this central peak seems to indicate the presence of the HBT effect.

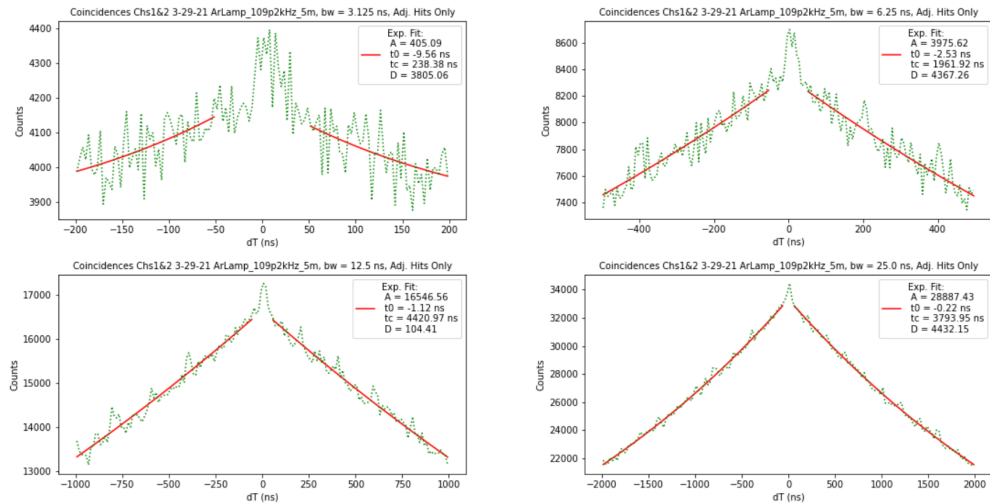


Figure 10: These are the four middle-range (200 ns, 500 ns, 1 μ s, 2 μ s) dT histograms from Fig. 9, with exponential fits overlaid. The fits ignore the central ± 50 ns on the x-axis to show the central HBT peak. In the legend, A represents the amplitude, t_0 the central location in x, t_c the characteristic decay time, and D the vertical offset from zero of the exponential.

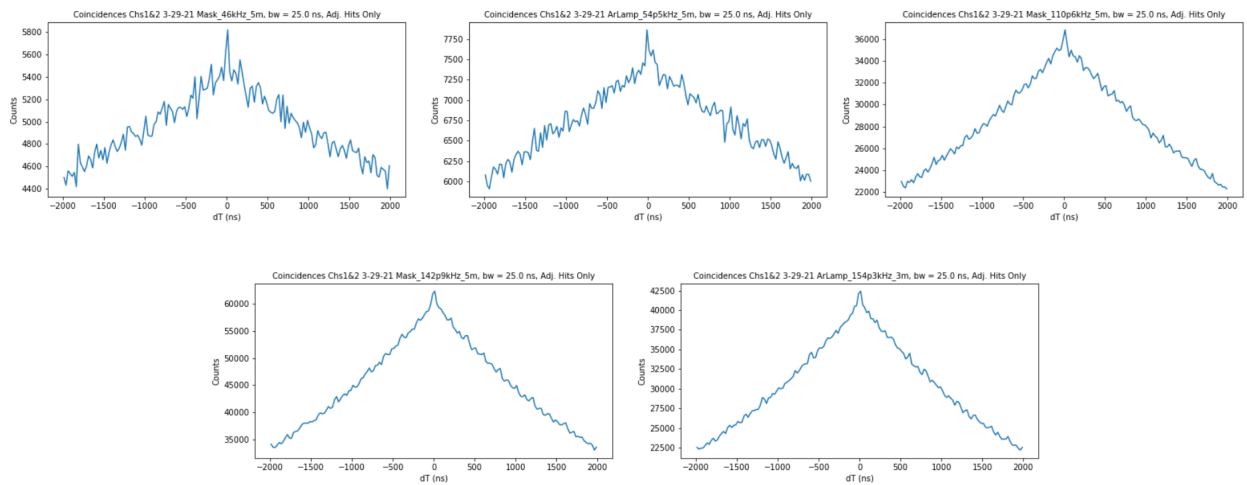


Figure 11: Coincidence histograms for five masked datasets with varying photon rates. From left to right, top to bottom, the rates are 46, 54, 110, 143, and 154 kHz. All histograms have a dT range of $\pm 2 \mu\text{s}$ and a bin width of 25 ns, and they are all 5 minutes in duration with the exception of the bottom-right one, which is 3 minutes.

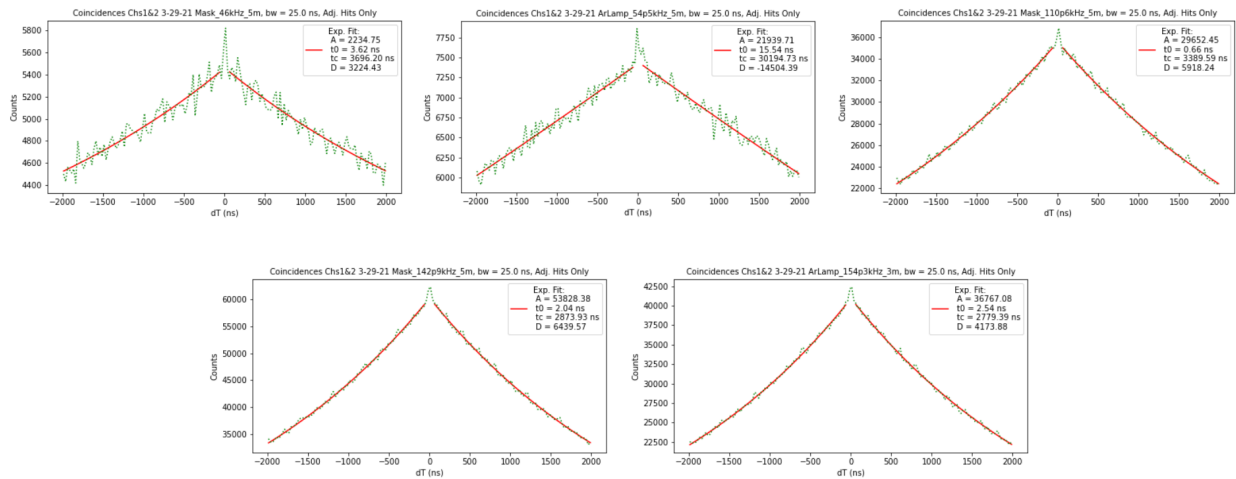


Figure 12: The same coincidence histograms from Fig. 11, with exponential fits overlaid. As before, these fits ignore the central ± 50 ns and only fit the exponential tails.

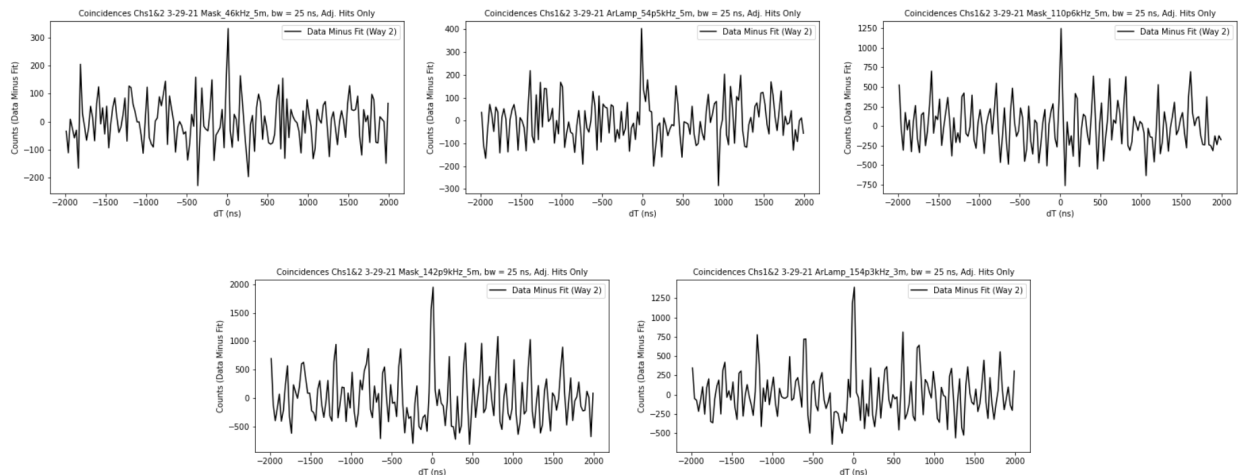


Figure 13: The same coincidence histograms from Figs. 11 and 12, but this time plotting the difference between the data and the exponential fit (data minus fit). Note that the fits used here are not the same as those in Fig. 12; instead, here we take into account the entire coincidence distribution, including the central ± 50 ns, when determining the optimal fit parameters. Hence the fits used in these plots represent the best possible exponential fit to the data. Even so, it is apparent that the fits are very poor near the central peak. We interpret this as strong evidence that the coincidence data itself is not inherently exponential, but rather has a Gaussian component centered near zero and overlaid on top, which we attribute to the presence of the HBT effect.

potentially be used for the first tests of our design with multiple spectral bins in each detector. We also have plans to double the number of channels on the Tpx3Cam setup from two to four, which if paired with an adjustable phase delay would allow us to look for two-photon amplitude interference with the camera as well. All of these steps should pave the way for eventual observational tests of our setup with astronomical sources.

3 Conclusion

We have discussed ongoing proof-of-concept testing of a novel optical interferometer that bypasses the classical requirement of maintaining a live connecting path between stations during observation, and as a result would achieve angular resolution improved by several orders of magnitude. We described tests of two different imaging candidates for this telescope: SNSPDs, and the fast optical camera Tpx3Cam. We have observed the HBT effect in data from both the nanowire and camera setups, and we also have a $3.88 \pm 0.92\sigma$ result indicating that our observed coincidence correlations in the nanowire setup are due to a real two-photon amplitude interference effect, rather than chance correlations arising from uncorrelated data. Finally, we

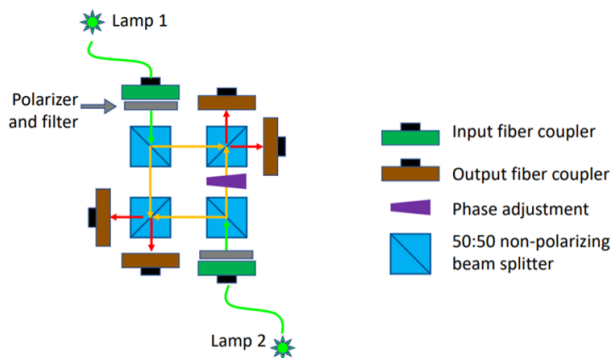


Figure 14: Diagram of the in-progress free-space implementation of the nanowire setup. This setup is effectively the same as that shown in Fig. 2, except that the optical fibers that the light propagates through have been replaced by free space to provide improved phase stability and control.

described our plans for future tests of the telescope design, including improving the phase stability of the nanowire setup and upgrading both setups to have more channels. Once these modifications have been completed and tested, we can begin collecting the first real astrometric data with this design, which has applications in many active areas of astronomical study.

Acknowledgments

This project was supported in part by the U.S. Department of Energy, Office of Science, Office of Workforce Development for Teachers and Scientists (WDTS) under the Science Undergraduate Laboratory Internships Program (SULI). We would like to thank our mentor, Andrei Nomerotski, for educating us on the details of the project and for guidance throughout. We also thank members of the BNL QIST research group, including Paul Stankus, Stephen Vintskevich, Denis Dolzhenko, and Michael Keach, for the same reasons. We thank our team leader, Sal Gonzalez, for support throughout the project period, and we also gratefully acknowledge financial support from the Department of Energy through its SULI program, without which we would not have gotten this opportunity or produced this work. Thank you!

A Pearson correlation coefficient error propagation

In this appendix we demonstrate the error propagation steps, assuming Poissonian error in the number of coincidences:

$$r(\mathbf{x}, \mathbf{y}) = \frac{\sum_i^N (x_i - \bar{x})(y_i - \bar{y})}{\sqrt{\sum_i^N (x_i - \bar{x})^2 \sum_i^N (y_i - \bar{y})^2}}$$

$$\mathbf{x} = N(13)(t) + N(24)(t)$$

$$\mathbf{y} = N(14)(t) + N(23)(t)$$

1. $\sigma_{x_i} = \sqrt{x_i}$
2. $\sigma_{\bar{x}} = \frac{1}{N} \sqrt{\sigma_{x_i}^2 + \dots + \sigma_{x_N}^2}$
3. $\sigma_{(x_i - \bar{x})} = \sqrt{(\sigma_{x_i})^2 + (\sigma_{\bar{x}})^2}$
4. $\sigma_{(x_i - \bar{x})(y_i - \bar{y})} = (x_i - \bar{x})(y_i - \bar{y}) \sqrt{\left(\frac{\sigma_{x_i - \bar{x}}}{x_i - \bar{x}}\right)^2 + \left(\frac{\sigma_{y_i - \bar{y}}}{y_i - \bar{y}}\right)^2}$
5. $\sigma_{\sum (x_i - \bar{x})(y_i - \bar{y})} = \sqrt{\sigma_{(x_1 - \bar{x})(y_1 - \bar{y})}^2 + \dots + \sigma_{(x_N - \bar{x})(y_N - \bar{y})}^2}$
6. $\sigma_{(x_i - \bar{x})^2} = 2(x_i - \bar{x})\sigma_{(x_i - \bar{x})}$
7. $\sigma_{\sum (x_i - \bar{x})^2} = \sqrt{\sigma_{(x_1 - \bar{x})^2}^2 + \dots + \sigma_{(x_N - \bar{x})^2}^2}$
8. $\sigma_{\sum (x_i - \bar{x})^2 \sum (y_i - \bar{y})^2} = \sum (x_i - \bar{x})^2 \sum (y_i - \bar{y})^2 \sqrt{\left(\frac{\sigma_{\sum (x_i - \bar{x})^2}}{\sum (x_i - \bar{x})^2}\right)^2 + \left(\frac{\sigma_{\sum (y_i - \bar{y})^2}}{\sum (y_i - \bar{y})^2}\right)^2}$
9. $\sigma_{\sqrt{\sum (x_i - \bar{x})^2 \sum (y_i - \bar{y})^2}} = \frac{1}{2\sqrt{\sum (x_i - \bar{x})^2 \sum (y_i - \bar{y})^2}} \sigma_{\sum (x_i - \bar{x})^2 \sum (y_i - \bar{y})^2}$
10. $\sigma_r = r \sqrt{\left(\frac{\sigma_{\sum (x_i - \bar{x})(y_i - \bar{y})}}{\sum (x_i - \bar{x})(y_i - \bar{y})}\right)^2 + \left(\frac{\sigma_{\sqrt{\sum (x_i - \bar{x})^2 \sum (y_i - \bar{y})^2}}}{\sqrt{\sum (x_i - \bar{x})^2 \sum (y_i - \bar{y})^2}}\right)^2}$

B Additional results from SNSPD experiments

B.1 After-pulsing

After-pulsing refers to the deficiency in SNSPDs that they will occasionally repulse after a real photon detection leading to an artificial detection [6]. To improve analysis, it is desirable to identify and remove after-pulses so that coincidence distributions only consider actual photon detections and not these artificial after-pulses. Fortunately, after-pulse events are typically easily identifiable and corrected for since they tend to come shortly after legitimate photon detection (on the order of 100 ns). To correct for after-pulsing, a cut-off can be introduced so that all detection events that are within a predetermined time window after a

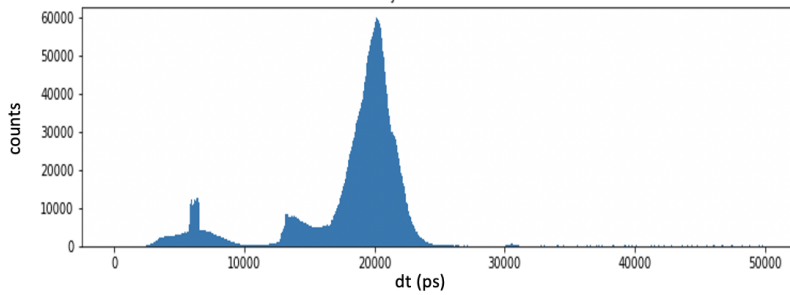


Figure 15: A sample plot showing the time difference between consecutive hits in one of the SNSPD channels. The after-pulsing region is clearly less than 30 ns, as there is a marked increase in consecutive detections within this window.

previous detection are disregarded. For our current experimental implementation, the after-pulsing effect is clearly demonstrated in Figure ?? in which there is a significant spike in the number of events that are detected within 20-30 ns of a prior detection. Therefore, to correct for after-pulsing, a cut-off was introduced at 30-35 ns for all of our analyses. These timing and rate of after-pulsing is similar to that which was observed with SPDC sources in experiments performed in October 2020.

B.2 Visibility and fiber delays

As can be seen in Figure 3, the HBT peak is not centered at a time difference at or near 0 ns between detected photons. This is due to an additional fiber that is inserted after the final beam splitter and before one of the detectors. One may therefore be worried that these additional fibers in one of the channels can reduce the visibility. However, as seen in Figure 16, there is no appreciable impact on the visibility when the fiber delay is changed between channels or when it is removed entirely.

B.3 Visibility dependence on polarizers

Almost all long run experiments conducted thus far have been without polarizers on the lamps. As can be seen in Figure 17, polarizers improve the visibility on the the HBT effect by a factor of about two. The improved visibility when polarizers are included may make it worthwhile to conduct future long-run experiments with polarizers. It is worth noting that one such experiment was conducted. However, as can be seen in Figure 18, this experiment had significant phase instability. In order to use polarizers in future

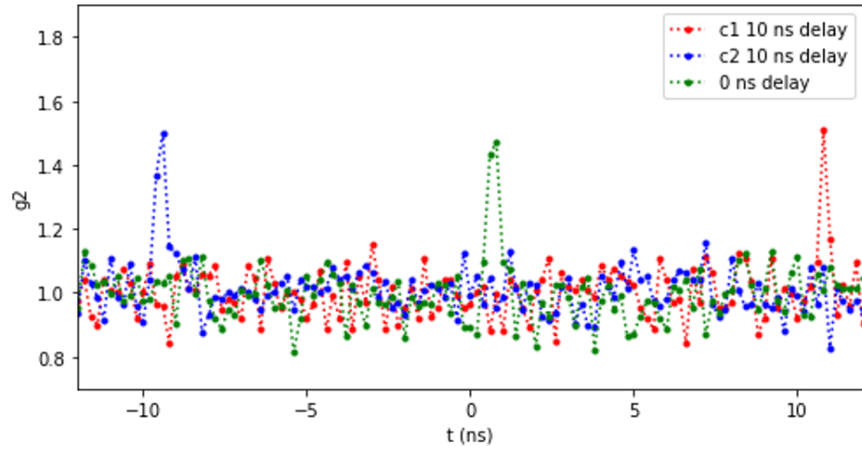


Figure 16: Results from single lamp experiments with Polarizers and with delays swapped between channels and removed entirely.

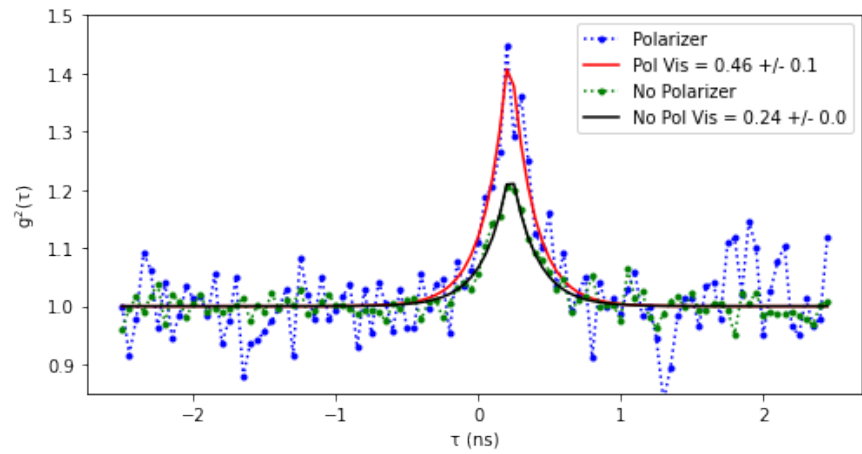


Figure 17: Comparisons of g^2 distributions with and without polarizers.

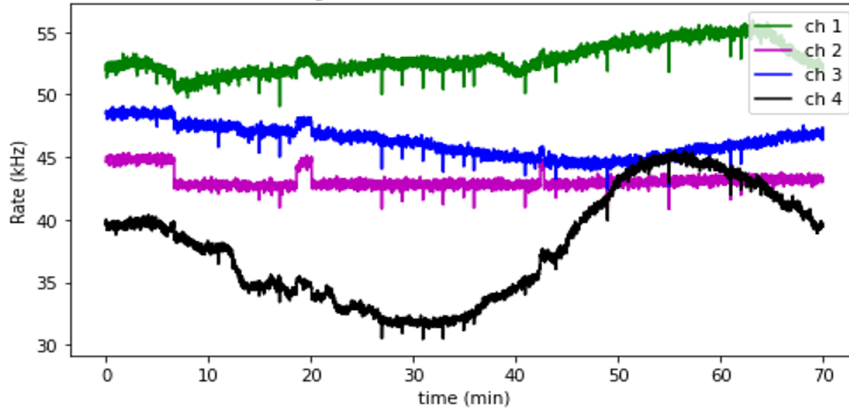


Figure 18: Singles rates from 70 minute experiments with polarizers on each lamp. Long time-scale phase instability is readily observable.

two-photon amplitude interference experiments, this issue needs to be addressed.

B.4 Mach-Zehnder setup and tracking phase stability

Another experimental setup that has been explored is shown in Figure 19. This experiment introduces a Mach-Zehnder (MZ) connection and is similar to the schematic in Figure 2, but with an additional beam splitter inserted after one of the lamps. As seen in the singles rates shown in Figure 20, the MZ connection allows us to clearly track the phase stability over the course of the experiment. This additional MZ connection may be used in the future to either correct for phase wandering in real time or to measure phase instability after the fact to inform analysis and improve the experimental setup.

B.5 Additional correlation and two-photon amplitude interference analysis

B.5.1 Determining windows for the peak and normalization regions

Figure 3 provides a rough picture of the peak and normalization coincidence ranges. The shape of each coincidence distribution, is a convolution of a Gaussian (detector resolution) and Exponential (Argon transition line-width). For simplicity, to identify the center and approximate width of the peak, distributions are fit with a simple Gaussian, as shown in Figure 21. A numerical scan using different σ ranges found that a $\pm 1.5 \sigma$ range led to the strongest correlation/anti-correlation signal. This corresponds to $\pm \approx 200$ ns window. The detector resolution is known to be on the order of 100 ps [3], and therefore this $\pm \approx 200$ ns window is in fact

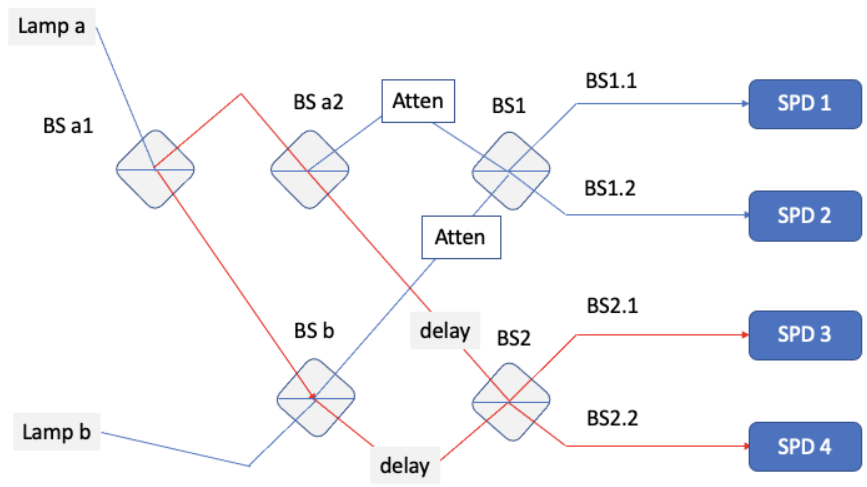


Figure 19: Schematic of the laboratory arrangement with a Mach-Zehnder connection included.

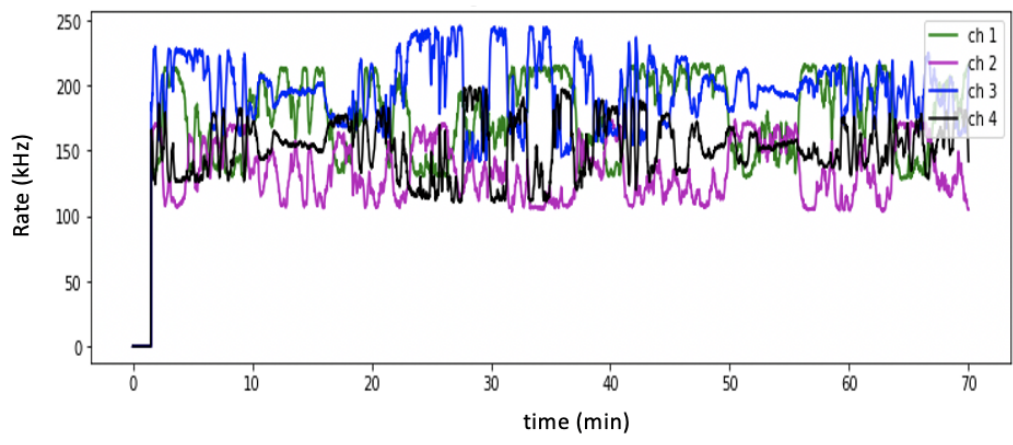


Figure 20: Singles rates from 70 minute experiments with the Mach-Zehnder connection included.

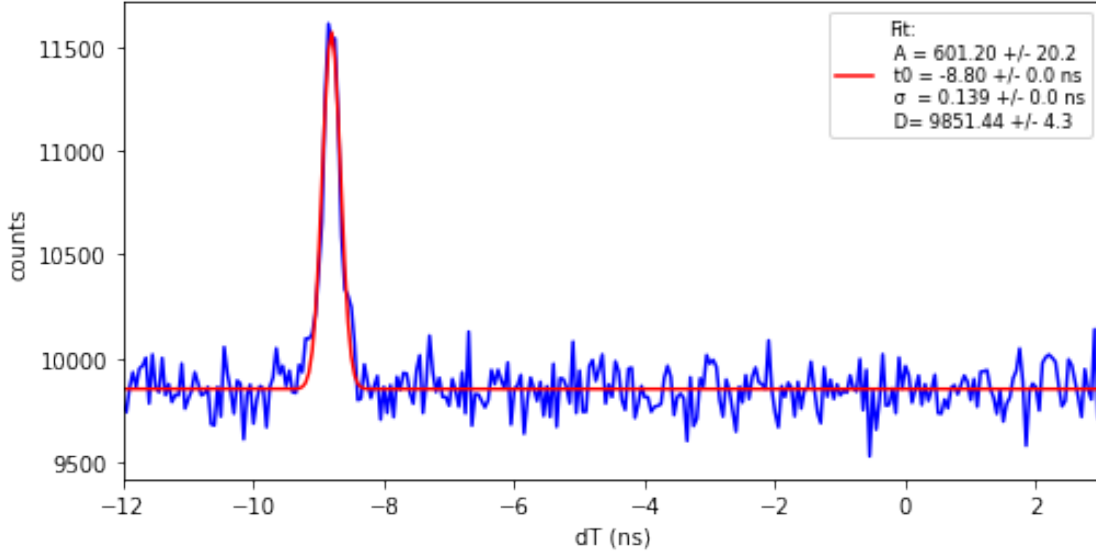


Figure 21: The coincidence distribution from Figure 3 fit with a Gaussian: $Ae^{-\left(\frac{t-t_0}{2\sigma}\right)^2} + D$

approximately a $\pm 2 \sigma_{res}$ window, where σ_{res} is the detector resolution. Future analyses may wish to find the correct fit with a convolution and adjust the peak and normalization ranges to be precisely $\pm 2 \sigma_{res}$.

B.5.2 Checking for systematic experimental biases

To determine that the two-photon amplitude interference effect is actually observed, it is important to confirm that the observed correlations and anti-correlations in the Pearson correlation coefficient are not systematic in the experimental setup. Figure 22 shows that the sign of the correlations between peak coincidence rates across all channel pairs accord with the predictions of the two-photon amplitude interference effect predicts. In Section 2.3.2, we employed a statistical analysis to determine the statistical significance of the observed correlations, but did not consider that the magnitude of the correlations (or anti-correlations) are due a systematic bias in the experiment. Here, we discuss the potential for this to be the case and show that the data rules out that the observed correlations are simply due to systematic effects.

To rule out systematic correlation bias across channel pairs, we can use the normalization region and analyze the correlations that are observed in this region. If the normalization regions show correlations similar to the peak region, it may indicate systematic biases, but if they show results that are consistent overall with zero correlation, it increases confidence that any observed correlations in the peak regions are not due to systematic effects.

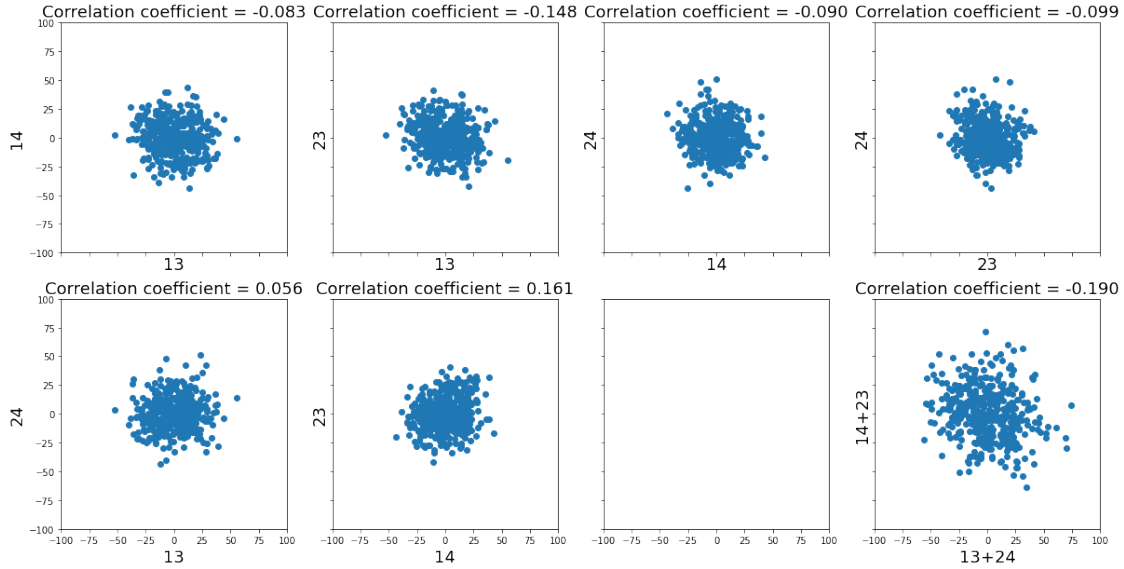


Figure 22: Scatter plots of the peak coincidence rates between various channel pair combinations with the correlation coefficient included. The scatter plot shows the number of peak coincidences minus the mean rate. The bottom right plot shows the averaged deviation from the mean across the two channel pairs on each axis. As predicted by the two-photon amplitude interference effect, the only two positively correlated channel pairs are 1&3-2&4 and 1&4-2&3. All other channel pairs show a negative correlation, as expected.

The top right plot in Figure 6 shows the rate of normalization coincidences when the window is set to $\pm 10 \sigma$ and averaged down to $\pm 1.5 \sigma$ to smooth over fluctuations in the normalization region. However, for the purposes of determining whether there are systematic correlations in the experimental setup, it is useful to use a non-averaged normalization window that is identical in size to the peak coincidence window. Figure 23 shows the rate of normalization coincidences when the window is set to match the peak window of $\pm 1.5 \sigma$. It is worth noting that a comparison of the $g^2(0)$ distributions when the normalization window is $\pm 10 \sigma$ and when it is $\pm 1.5 \sigma$, shown in Figure 24, reveal that the peak coincidence rate is generally higher than the normalization coincidence rate when the normalization window is averaged over a $\pm 10 \sigma$ (as is expected due to the HBT effect). However, when a $\pm 1.5 \sigma$ window is used for the normalization region, channel pairs 2&3 and 2&4 show no HBT enhancement at all. It is not currently clear why this is the case, and it is worthwhile to study more closely whether there are any algorithmic or analytical issues that are incorrectly and artificially destroying the HBT signal for some channel pairs.

We now turn to correlations between channel pairs in the normalization window to determine if there are any systematic biases in our experiment. Figure 25 shows the scatter plots and correlation coefficients for the normalization regions for each channel combination for a $\pm 1.5 \sigma$ window. These results

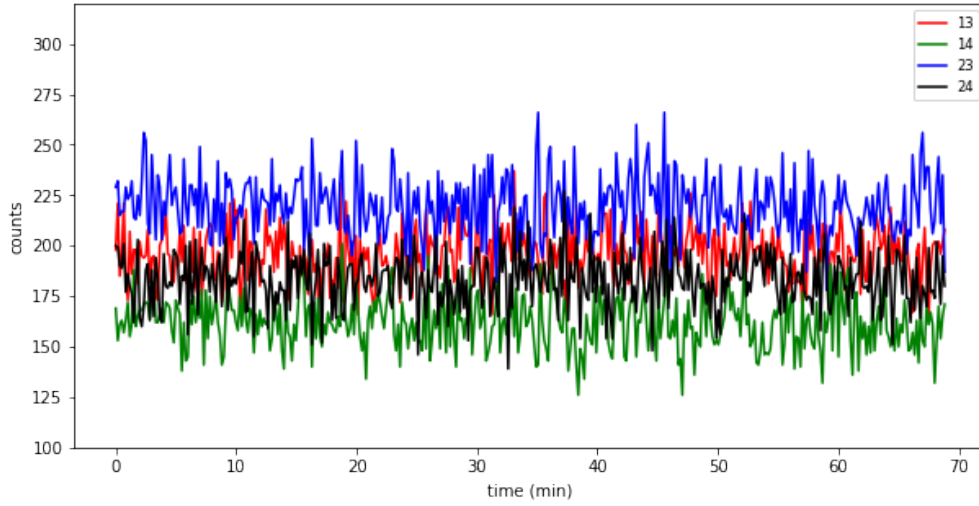


Figure 23: Normalization coincidence rates when the window is set to $\pm 1.5 \sigma$ (equal to the window used for the peak coincidence region).

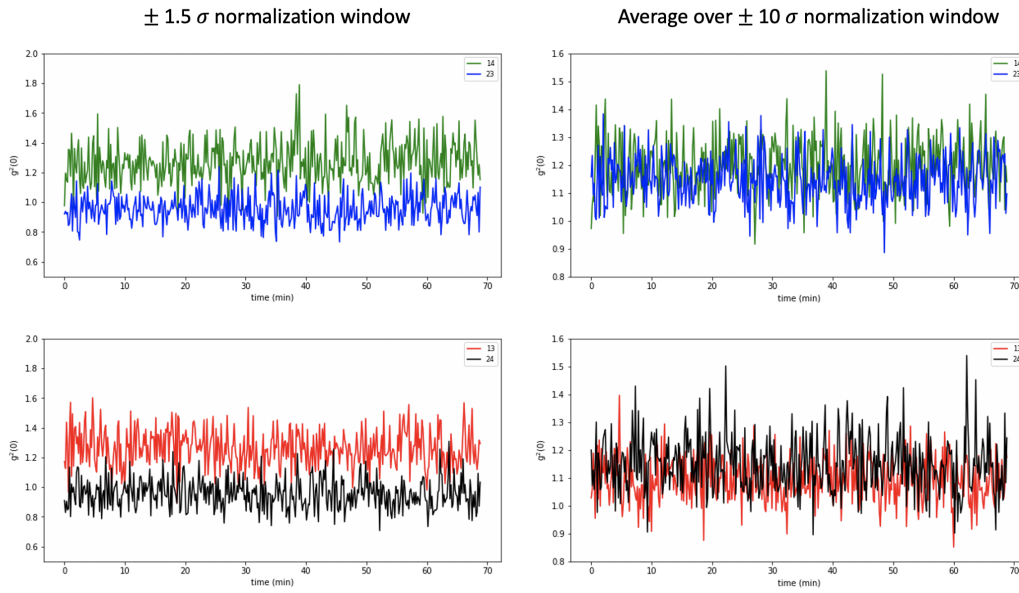


Figure 24: $g^2(0)$ distributions over the duration of the 70 minute experiment. Left: $\pm 1.5 \sigma$ window for the normalization coincidence region and the peak coincidence region. Right: $\pm 10 \sigma$ window for the normalization coincidence region that is averaged down to a $\pm 1.5 \sigma$ and $\pm 1.5 \sigma$ for the peak coincidence region.

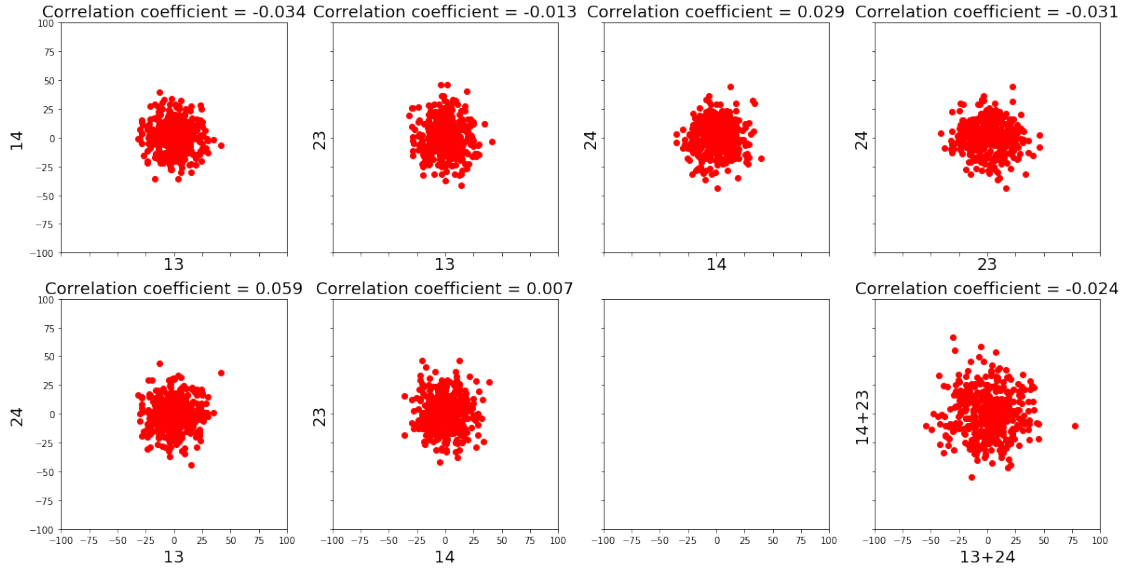


Figure 25: Scatter plots of the normalization coincidence rates between various channel pair combinations with the correlation coefficient included. The scatter plot shows the number of correlation coincidences minus the mean rate. The bottom right plot shows the averaged deviation from the mean across the two channel pairs on each axis. These results are generally consistent with a null correlation across all channel pairs in the normalization region.

show that the normalization region does not show a consistent bias towards the correlations predicted by the two-photon amplitude interference, and the overall correlations that are present are comparatively small and may therefore be considered as consistent with the expected null correlation across all channel pairs.

With the confidence that the correlations are not due to a systematic effect, we can use the smoothed over $\pm 10 \sigma$ window for the normalization region to create similar scatter plots for the $g_2(0)$ distributions. As shown in Figure 26, the $g_2(0)$ results also indicate that correlations have been observed which are consistent with the predictions of the two-photon amplitude interference effect.

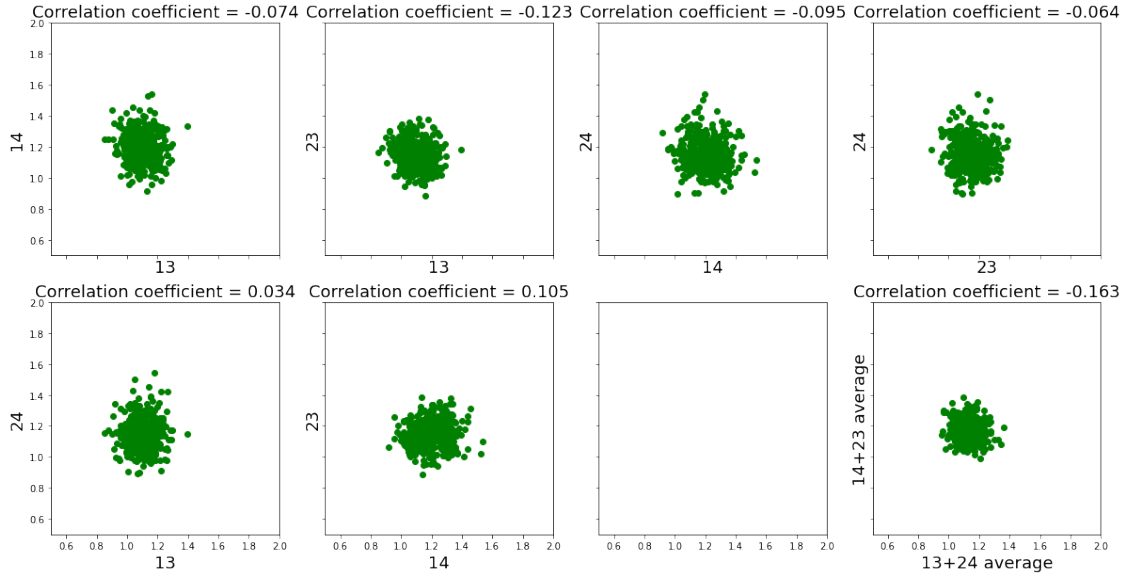


Figure 26: Scatter plots of $g^2(0)$ distributions between various channel pair combinations with the correlation coefficient included. These results further affirm the agreement between observed correlations and those predicted by the two-photon amplitude interference effect.

References

- [1] Stankus, P., Nomerotski, A., Složar, A., and Vintskevich, S., “Two-photon amplitude interferometry for precision astrometry,” *arXiv preprint arXiv:2010.09100* (2020).
- [2] Brown, R. H. and Twiss, R. Q., “A test of a new type of stellar interferometer on sirius,” *Nature* **178**, 1046–1048 (Nov. 1956).
- [3] Nomerotski, A., Stankus, P., et al., “Quantum-assisted optical interferometers: Instrument requirements,” *Proc. SPIE 11446, Optical and Infrared Interferometry and Imaging VII*, *arXiv:2012.02812* (Dec. 2020).
- [4] Schuck, C., Pernice, W. H. P., and Tang, H. X., “Waveguide integrated low noise nbtin nanowire single-photon detectors with milli-hz dark count rate,” *Sci. Rep.*, *3*, 1893 (May 2013).
- [5] Nomerotski, A., “Imaging and time stamping of photons with nanosecond resolution in Timepix based optical cameras,” *arXiv preprint arXiv:1902.01357* (2019).

- [6] Burenkov, V., Xu, H., Qi, B., Hadfield, R. H., and Lo, H.-K., “Investigations of afterpulsing and detection efficiency recovery in superconducting nanowire single-photon detectors,” *Journal of Applied Physics*, *113*, 213102 (May 2013).